catalysts

MDPI

Article

The Effect of Atomic Layer Deposited Overcoat on Co-Pt-Si/γ-Al_2O_3 Fischer–Tropsch Catalyst

Niko Heikkinen [1,*], Laura Keskiväli [1], Patrik Eskelinen [1], Matti Reinikainen [1] and Matti Putkonen [2]

[1] VTT Technical Research Centre of Finland, P.O. Box 1000, FIN-02044 VTT Espoo, Finland; laura.keskivali@vtt.fi (L.K.); patrik.eskelinen@vtt.fi (P.E.); matti.reinikainen@vtt.fi (M.R.)
[2] Department of Chemistry, University of Helsinki, P.O. Box 55, FI-00014 Helsinki, Finland; matti.putkonen@helsinki.fi
* Correspondence: niko.heikkinen@vtt.fi; Tel.: +358-20-7225-420

Abstract: Atomic layer deposition (ALD) was used to prepare a thin alumina layer on Fischer–Tropsch catalysts. Co-Pt-Si/γ-Al_2O_3 catalyst was overcoated with 15–40 cycles of Al_2O_3 deposited from trimethylaluminum (TMA) and water vapor, followed by thermal annealing. The resulting tailored Fischer–Tropsch catalyst with 35 cycle ALD overcoating had increased activity compared to unmodified catalyst. The increase in activity was achieved without significant loss of selectivity towards heavier hydrocarbons. Altered catalyst properties were assumed to result from cobalt particle stabilization by ALD alumina overcoating and nanoscale porosity of the overcoating. In addition to optimal thickness of the overcoat, thermal annealing was an essential part of preparing ALD overcoated catalyst.

Keywords: Fischer–Tropsch synthesis; cobalt catalyst; atomic layer deposition; ALD; cobalt on alumina; annealing; catalyst overcoating

Citation: Heikkinen, N.; Keskiväli, L.; Eskelinen, P.; Reinikainen, M.; Putkonen, M. The Effect of Atomic Layer Deposited Overcoat on Co-Pt-Si/γ-Al_2O_3 Fischer–Tropsch Catalyst. *Catalysts* **2021**, *11*, 672. https://doi.org/10.3390/catal11060672

Academic Editors: Leonarda Francesca Liotta and Morris D. Argyle

Received: 5 May 2021
Accepted: 23 May 2021
Published: 24 May 2021

1. Introduction

Fischer–Tropsch (FT) is a flexible synthesis route that converts synthesis gas into liquid fuels and chemicals [1–3]. Recently, the use of biomass, waste, or gaseous side streams as feedstock have gained much interest [4]. To create value from renewable feedstocks with Fischer–Tropsch technology, catalyst development has a significant role to play. Numerous studies have shown effects of catalyst support [5–7], promoter [7–10], and active phase particle size [11–13] on FT catalyst activity. Although these factors are well documented, challenge remains to keep the catalyst in the desired state during reduction and FT reaction. Atomic layer deposition (ALD) provides a pathway to create nanoscale overcoating for protection of active sites and to stabilize them in the most suitable form [3]. ALD is an excellent tool for catalytic solutions due to its ability to produce conformal and ultrathin layers on various support materials and shapes [3,14,15]. While ALD has many advantages for catalyst preparation, challenges might arise with highly porous supports [16,17]. Precursor diffusion into the narrow pores and ligand removal reactions take longer time with high surface area and aspect ratios compared to smooth, non-porous surfaces [18]. In addition, although ALD overcoatings are considered as conformal films on planar substrates, uneven island growth might occur with catalyst samples [19]. This overcoating island growth results from varying growth regimes depending on the number of deposited cycles, favoring specific surface locations especially at initial ALD cycles (<30 cycles) [20]. Despite these challenges, ALD offers an interesting tool for catalyst preparation with precise control of deposited material composition, size, and structure.

The ALD process is a cyclic deposition method with self-limiting reactions between the gas phase precursors and substrate surface. Figure 1 presents a schematic illustration of an atomic layer deposition cycle for Al_2O_3. In the first step, trimethylaluminum (TMA) is pulsed to the surface and during a gas–solid reaction, O-Al$(CH_3)_2$ structures are formed on

the surface, releasing methane as a by-product. During the water pulse, hydroxyl structures are formed on the surface and again CH_4 is released as a by-product. After each precursor pulse, any excess precursors and methane are removed by inert purging.

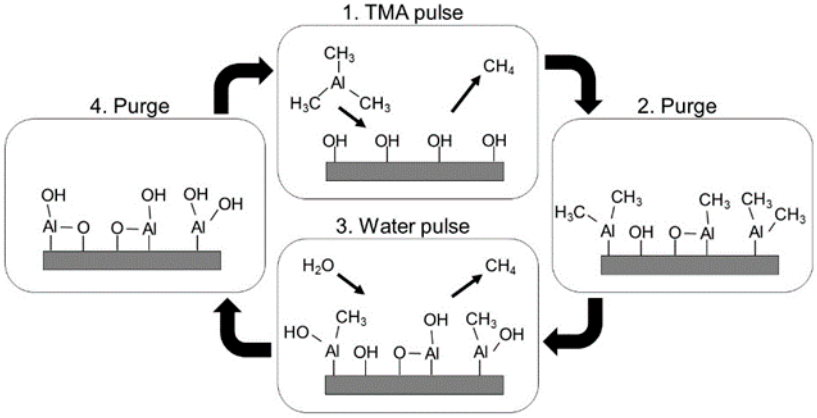

Figure 1. Atomic layer deposition cycle of the Al_2O_3 process.

Regarding ALD-enhanced heterogeneous catalysts, Lee et al. [21] have investigated the effect of TiO_2 overcoating on a Co/γ-Al_2O_3 catalyst with aqueous-phase hydrogenation reaction. Their results show that an overcoated TiO_2 layer inhibits catalyst deactivation by preventing leaching and sintering of the active phase. Interestingly, when Al_2O_3 was used instead of TiO_2 as overcoat material, they reported a decrease in catalytic activity. It was assumed that the use of alumina resulted in partial formation of irreducible cobalt aluminate. In addition to cobalt aluminate formation, other studies have shown a decrease in catalytic activity by partial or full coverage of active centers upon application of a thick overcoat layer [22]. To overcome the decrease in catalytic performance due to active site coverage, there are methods to re-expose active sites. Liang et al. [23] describe a method using molecular layer deposition (MLD) with a ligand precursor as well as method with carbonaceous precursors [24]. To create void spaces and pores through the overcoat layer, excess ligands or carbonaceous precursors could be removed by solvents or an oxidative environment accompanied by increased temperature. An alternative and more common method is thermal treatment, where porosity is created by temperature ramp in inert atmosphere.

Several studies have investigated how thermally treated ALD overcoatings could be used to enhance catalyst properties in severe reaction conditions. Lu et al. [25] reported a method to inhibit deactivation by thermally treated ALD overcoating. They investigated the deactivation resistance of a Pd-catalyst in oxidative dehydrogenation of ethane, where 45 cycles of ALD alumina (TMA + H_2O) was deposited on the Pd-catalyst. The resulting catalyst was less prone to deactivation by coking and sintering and selectivity was shifted towards desired products. They explained how an ALD overcoating could selectively interact with the high-energy, low-coordination sites of the active metal believed to be responsible for particle sintering. Similar results were reported by Ma et al. [22], where Au/TiO_2 oxidation catalyst with amorphous SiO_2 overcoating exhibited increased thermal stability and activity. According to them, the thermally treated overcoating stabilized gold nanoparticles and created surface conditions less susceptible to cobalt crystallite migration and particle sintering. In these conditions, better activity could be expected, as to some extent, strong metal support interactions (SMSIs) are prohibited by atomic scale overcoating. In addition to the particle stabilization properties, the overcoated porous structure influences activity and selectivity as well. O'Neill et al. [26] reported that ALD deposited alumina binds preferably on low coordination sites, such as steps, creating pores mainly on terrace surfaces during thermal treatment. Through thermal annealing reformation of the overcoated surface, the solid surface is turned into a porous layer on top of the active metal sites and the support [21].

In this study, we examine the effect of ALD overcoatings on Fischer–Tropsch Co-Pt-Si/γ-Al_2O_3 catalysts prepared by incipient wetness impregnation [27]. Furthermore, we present the effect of varying ALD layer thickness and the temperature annealing method on catalyst activity and selectivity. To explain changes in catalyst performance, catalysts were characterized with physical adsorption-desorption (BET, BJH), in-situ X-ray diffraction (in-situ XRD), temperature-programmed reduction (TPR), static-H_2-chemisorption, and O_2-titration methods. Catalytic performance was studied using a tubular fixed-bed reactor system.

2. Results

2.1. Catalyst Characterization

Nitrogen Adsorption/Desorption

All catalysts exhibited a Gaussian-like pore size distribution. Surface areas ranged between 13–89 m^2 $gcat^{-1}$, pore volumes 0.03–0.24 mL $gcat^{-1}$ and average pore sizes 8.0–10.9 nm as shown in Table 1. The addition of ALD top coating noticeably decreased the physisorption values and after thermal annealing (TA) treatment, the values recovered. With the thickest 40c ALD overcoating, the surface area and pore volume were clearly lower compared to the other catalysts with thinner overcoats.

Table 1. Nitrogen sorption results for catalysts with and without thermal annealing (TA).

Catalyst	BET Surface Area (m^2 $gcat^{-1}$)	Pore Volume (mL $gcat^{-1}$)	Pore Size (nm)
Support (Puralox SCCa 5–150)	140	0.46	13.2
Catalyst	87	0.24	10.9
Catalyst + 15c + TA	88	0.23	10.5
Catalyst + 25c + TA	84	0.23	10.8
Catalyst + 35c + TA	89	0.24	10.7
Catalyst + 35c	13	0.03	8.0
Catalyst + 40c + TA	61	0.15	10.0

Experimental error ($\pm$ 2σ) for surface area was $\pm$ 1.2 m^2/g, pore volume $\pm$ 0.01 mL/g and pore size $\pm$ 0.1 nm. Uncertainty was determined from three independent runs for catalyst without overcoat.

ALD equipment and conditions have a significant effect on overcoat thickness. In our experiments, according to Si wafer reference, one deposition cycle corresponded approximately to 0.09 nm. This growth per cycle (GPC) is in line with the earlier studies [28]. As ALD cycle is regarded to produce conformal layer, 15, 25, 35, and 40 ALD cycles correspond to 1.35, 2.25, 3.15, and 3.60 nm thick coatings by calculation, respectively. The effect of added overcoat was clearly observed in the 35c catalyst without thermal annealing, where BET surface area, pore volume, and pore size were significantly decreased. This behavior was assumed to result from micropore filling and surface smoothening. After thermal annealing, BET surface area was increased back to similar level compared to the non-overcoated catalyst. This was a similar finding to the work of O'Neill et al. [3], who found that overcoat structure can be altered by thermal annealing duration and temperature.

2.2. Catalyst Reducibility

2.2.1. In-Situ X-ray Diffraction Results

In-situ XRD measurements were performed during thermal annealing and reduction. Results in Figure 2 show measured responses for (a) catalyst without overcoating and (b) catalyst + 35c ALD overcoating. Reduction from Co_3O_4 to CoO started already at 150 °C (after 2 h equilibrium time) in reducing gas flow.

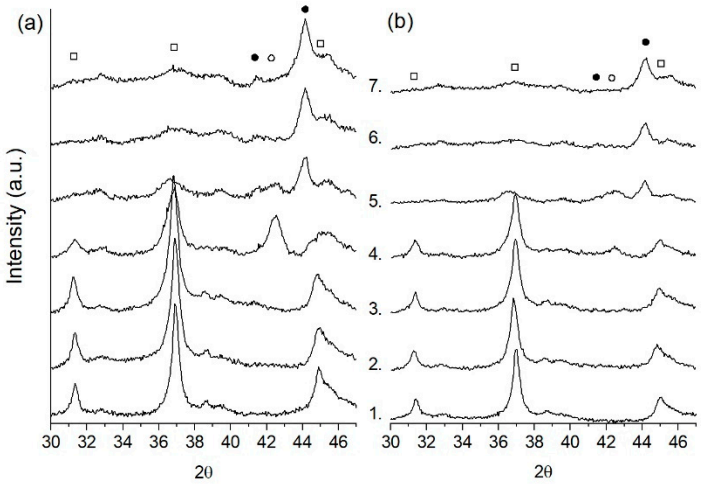

Figure 2. In-situ XRD results with thermal annealing and reduction program, (**a**) catalyst without overcoating and (**b**) catalyst + 35c ALD overcoating. Open rectangle symbol signifies Co_3O_4 species, open circle CoO, and black circle Co^0. Phase 1. measurement at 25 °C under N_2 flow; Phase 2. measurement after reaching thermal annealing temperature (420 °C, under N_2 flow); Phase 3. after cooldown to 150 °C and change to reducing gas (10% H_2 in N_2); Phase 4. after 2 h of reducing gas at 150 °C; Phase 5. after temperature increase for reduction (400 °C); Phase 6. after 4 h of reduction at 400 °C; Phase 7. after 6 h of reduction.

Metallic Co crystallite diameter was calculated from in-situ XRD measurement results (Table 2) with Scherrer equation (Equation (4)). In comparison to H_2-chemisorption Co^0 particle size, smaller Co^0 particle size values with in-situ XRD measurement was assumed to result from sample characteristics that are not considered with Scherrer equation, such as, defect concentration, crystalline strain, stacking faults, compositional variation, nanocrystallite size distribution, and sample thickness [29].

Table 2. Metallic and oxide cobalt particle size and cobalt dispersion data from X-ray diffraction and hydrogen chemisorption measurements. Catalyst with and without thermal annealing (TA).

	In-Situ XRD	H_2-Chemisorption			
Catalyst	**[a] Co_3O_4 Particle Size (nm)**	**[b] Co^0 Particle Size (nm)**	**H_2 Uptake (μmol $gcat^{-1}$)**	**[c] Co^0 Particle Size (nm)**	**[d] Cobalt Dispersion (%)**
Catalyst	14.5	7.8	69	14	6.7
Catalyst + 15c + TA	-	-	47	5	20.2
Catalyst + 25c + TA	-	-	46	5	19.5
Catalyst + 35c + TA	13.	8.3	58	11	9.0
Catalyst + 40c + TA	-	-	34	6	16.4

[a] Co_3O_4 in-situ XRD result before reduction. [b] Co^0 particle size measured with in-situ XRD after reduction. [c] Co^0 particle size determined from H_2-chemisorption result. [d] Cobalt dispersion calculated with Equation (5).

2.2.2. Hydrogen Chemisorption

Table 2 gives the dispersion and particle size values from in-situ XRD and static H_2-chemisorption measurements. Cobalt dispersion is determined from catalysts reduced at 400 °C. The dispersion for non-overcoated catalyst is 6.7% and with overcoated catalysts from 9% to 20.2%. As cobalt dispersion is varying with overcoat thickness, consequently the particle size fluctuated between 6–14 nm. Several studies have presented the effect of cobalt particle size on catalyst activity [11,12,30,31] and according to H_2-chemisorption result in Table 2, 35c + TA catalyst most favorable particle size from overcoated catalysts.

Pt and Si as catalyst promoters were presumed to have an insignificant effect on the produced overcoat. ALD overcoat reformation through thermal annealing was assumed

to reveal the active cobalt particles only partly for H_2-chemisorption, thus increasing the calculated dispersion value. It was suggested that ALD overcoating influenced determined dispersion and particle size through Co particle confinement. As amorphous ALD overcoating has no clear response in XRD, only minute deviation was found between non-overcoated catalyst (7.8 nm) and 35c + TA catalyst (8.3 nm). Different to XRD, H_2-chemisorption directly interacted with available metallic cobalt sites, indicating particle confinement effect in Table 2 Co^0 particle size approximation with H_2-chemisorption.

2.2.3. Temperature-Programmed Reduction (TPR)

The temperature-programmed reduction results presented in Table 3 show the extent of reduction for each sample. First, TPR was performed on the non-overcoated catalyst until 900 °C (Figure 3). Full cobalt reduction was assumed at this temperature and the extent of reduction was determined by dividing the hydrogen consumption $\leq$ 400 °C (reduction temperature) by the total hydrogen consumed at 900 °C. Secondly, non-overcoated catalyst total hydrogen consumption was used to determine the extent of reduction for the ALD samples. As ALD overcoating clearly inhibited complete Co reduction (Figure 4), the quantity of adsorbed hydrogen was compared to the total amount measured with the catalyst without overcoating.

Table 3. O_2-titration and TPR data for degree of reduction. Untreated catalyst and ALD overcoated catalyst after thermal annealing (TA).

Catalyst	Extent of Reduction (%)	
	O_2 Titration	TPR
Catalyst	62.6	57.7
Catalyst + 15c + TA	1.8	13.1
Catalyst + 25c + TA	3.8	16.9
Catalyst + 35c + TA	15.7	35.8
Catalyst + 40c + TA	1.4	11.7

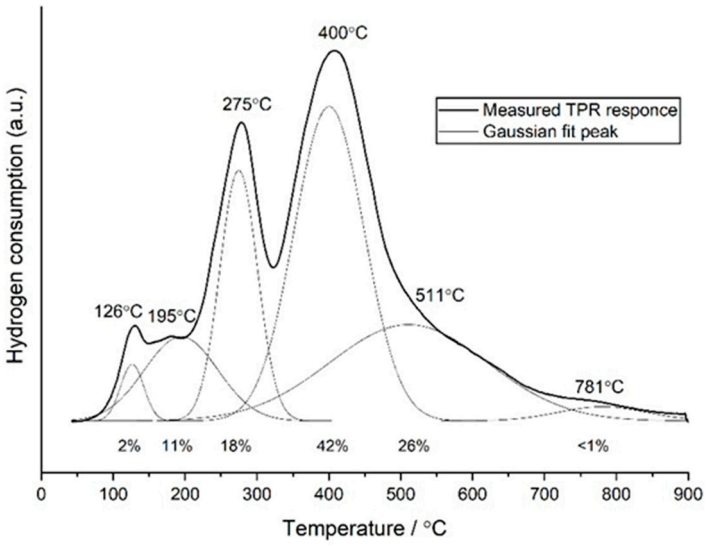

Figure 3. TPR measurement results for Co-Pt-Si/γ-Al_2O_3 catalyst with cumulative Gaussian fitted model, corresponding temperatures for each peak and hydrogen consumption percentage.

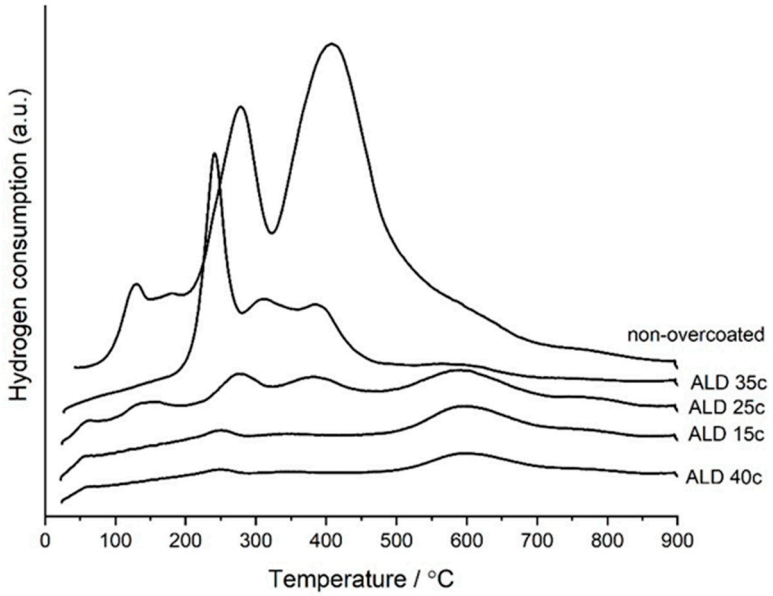

Figure 4. TPR curves for non-overcoated catalyst and ALD overcoated catalysts with thermal annealing (TA).

Gaussian peak deconvolution was used to determine six distinctive reduction peak positions. Figure 3 presents the results, where the first two peaks at temperature 126 °C and 195 °C relate to the nitrate residue reduction from the catalyst $Co(NO_3)_2$ precursor [32,33]. The peak at 275 °C was attributed to Co_3O_4 reduction to CoO and the peak at 400 °C to CoO reduction to metallic Co. Peaks found at temperatures 511 °C and 781 °C correspond to reduction of mixed cobalt-support complexes [32,34].

Lower hydrogen consumption was measured for all overcoated catalysts. Particularly, 15c and 40c overcoat catalysts consume significantly less hydrogen in TPR. Lee et al. [21] presented with an ALD overcoated catalyst ($Al_2O_3/Co/\gamma$-Al_2O_3) in aqueous phase reaction that irreducible cobalt aluminate was formed during calcination process. Our results could support this finding as 15c, 25c, and 40c catalysts have hydrogen consumption peak at 600 °C. Interestingly, the 35c catalyst showed different trend as hydrogen consumption was higher and peak at 600 °C was suppressed compared to other ALD catalysts.

2.2.4. Oxygen Titration

Prior to oxygen titration, the samples were reduced with hydrogen flow at 400 °C. After reduction, helium was used as a purge and carrier gas. Temperature was increased to 450 °C and oxygen pulses were introduced to the sample until no consumption was measured by the thermal conductive detector (TCD). Reduction is a two-step process that propagates according to Equation (1) and Equation (2).

$$Co_3O_4 + H_2 \rightarrow 3CoO + H_2O \quad (1)$$

$$3CoO + 3H_2 \rightarrow 3Co + 3H_2O \quad (2)$$

Oxygen titration was assumed to follow a reversible stoichiometry.

According to Ma et al. [22], ALD treatment can partially or fully cover catalyst active sites upon overcoating. Table 3 results seem to support their finding, as oxygen consumption was much lower for ALD overcoated catalysts. For this reason, the extent of reduction of the ALD catalysts as presented in Table 3 was underestimated compared to the TPR results. Interestingly, catalyst + 35c + TA had significantly higher O_2 consumption, which would indicate that, compared to other overcoated catalysts, more active sites were open after thermal annealing (TA) process.

2.3. Fischer–Tropsch Activity and Selectivity

Low conversion level (<16%) was important for preventing mass and energy transfer limitations. Furthermore, temperature differences in catalyst bed were minimized by catalyst bed silicon carbide dilution. In the reaction experiments, mass transfer limitations were shown to be negligible by varying reaction flow. In Figure 5, CO conversion as a function of space-time ($GHSV^{-1}$) showed linear behavior, which would indicate that experimental results provided reliable comparative information between catalysts.

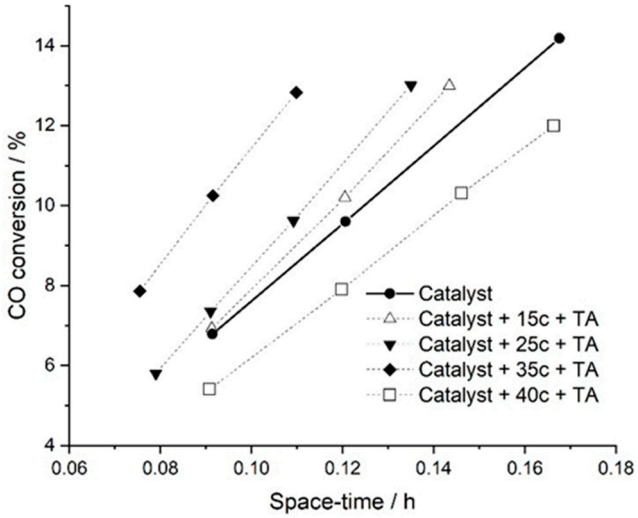

Figure 5. Effect of ALD overcoating thickness on catalyst activity. Activity presented as carbon monoxide conversion as a function of space-time.

Figure 5 presents the reaction experiment results, with the 15c and 25c catalysts showing a slight CO conversion increase at space-time 0.09 h. However, with the catalyst + 35c + TA, the conversion increases from 6.7% to 10.3%. Figure 6 gives the initial activity phase in identical reaction conditions without space-time or gas hourly space velocity normalization.

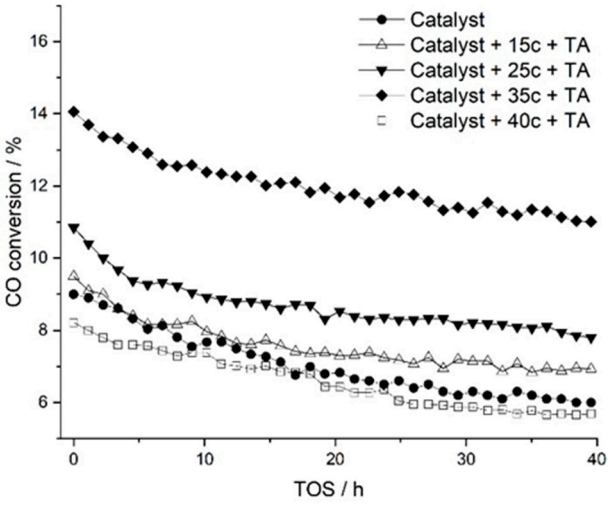

Figure 6. Catalyst overall activity during reaction start-up phase and stabilization during 40-h time-on-stream with fixed reaction conditions (200 °C, 20 bar, and total flow 6.6 nL h^{-1}). Catalyst bed containing 603, 603, 613, 609, and 601 mg of catalyst respectively to non-overcoated catalyst, 15c, 25c, 35c, and 40c catalysts.

In addition to online carbon monoxide conversion monitoring, a complete mass balance was determined by combining online and offline measurements from gaseous, oil and wax fractions. As the hot and cold trap separated the overlapping hydrocarbon

fractions, the mass balance was determined from gaseous online samples and offline analysis results were fitted to the total mass balance. The mass balance results are presented in Figure 7 as hourly hydrocarbon production rate per mass of catalyst (g_{HC} $gcat^{-1}$ h^{-1}) and the space-time yield of C_{5+} hydrocarbons.

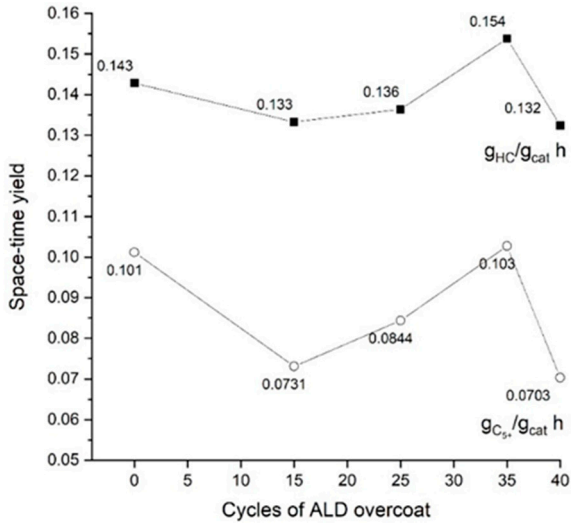

Figure 7. Space-time yield of hydrocarbons at varying ALD overcoating thickness. Space-time yield determined from samples with comparative feed flow and time-on-stream (space-time 0.09 h, TOS 40 h).

Figures 7 and 8 results indicate that a small variation in number of ALD cycles can lead to rather different selectivity (see Supplementary Material for olefin to paraffin selectivity). Especially 15c and 40c catalysts promoted light hydrocarbon formation. This was assumed to result from enhanced hydrogenation activity of olefinic intermediates and a less suitable environment for CH_x step polymerization. Catalysts with 25 and 35 cycle overcoating appear to have similar enhanced hydrogenation abilities while promoting intermediate polymerization. Interestingly, the turn-over frequencies (TOF) in Figure 9 are increasing with thickening overcoat. According to H_2-chemisorption (Table 2) and TPR results (Table 3), overcoated catalysts had fewer cobalt sites available compared to non-overcoated catalyst. Therefore, TOF suggests that although fewer sites were available, the sites open for reaction had increased activity. It must be noted that although the available sites had increased activity, 40c + ALD lowered the overall activity especially (see Figure 6).

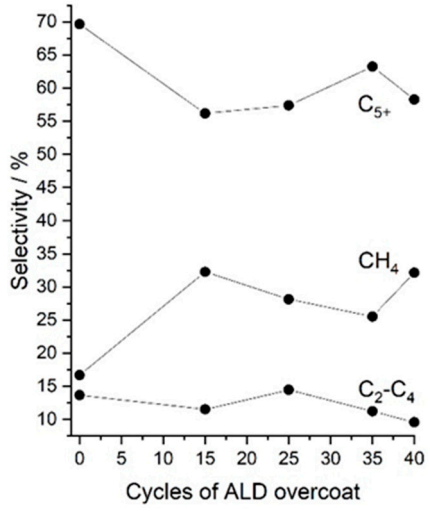

Figure 8. Methane, C_2-C_4 and C_{5+} selectivity as a function of ALD overcoat thickness. Data points selected from 9% carbon monoxide conversion level.

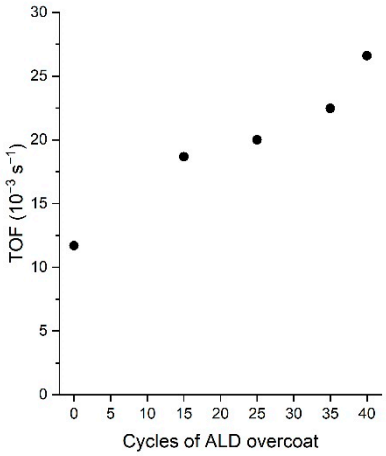

Figure 9. Turn over frequency (TOF) as a function of ALD overcoating cycles. TOF reported from ~9% carbon monoxide conversion for all catalysts.

Turn-over frequency was calculated with the equation

$$\mathrm{TOF} = \frac{x_{\mathrm{CO}} \cdot \dot{mol}_{\mathrm{CO}}}{mol_{\mathrm{Co}} \cdot s} \quad (3)$$

where x_{CO} is CO conversion, $\dot{mol}_{\mathrm{CO}}$ is carbon monoxide molar flow, and mol_{Co} is moles of available metallic cobalt determined by static H_2-chemisorption measurement.

2.4. Effect of ALD Overcoat and Thermal Annealing

According to reaction experiment results presented in Figure 10, thermal annealing (TA) was required to have increased activity for catalyst + 35c. When the thermal annealing process was applied prior to reduction, catalyst rate of reaction increased compared to non-thermal annealed ALD catalyst and non-overcoated catalyst.

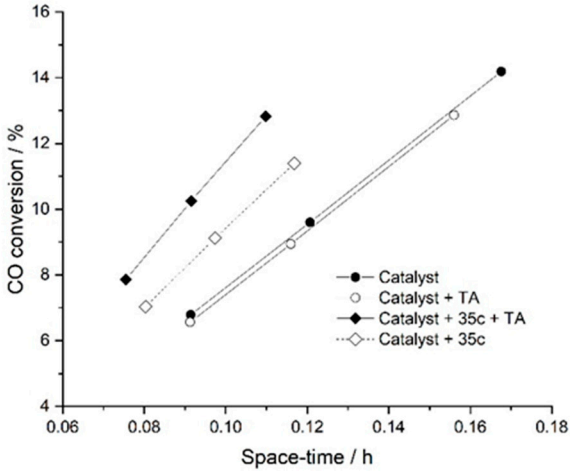

Figure 10. Effect of thermal annealing on catalyst activity. Activity presented as carbon monoxide conversion as a function of space-time.

In previous studies, the favorable effects of ALD overcoating on catalysts are explained by the nanoporous structure achieved with thermal annealing [3,25]. Porous coating stabilizes catalyst particles, while pores enable reactants to find their way onto the surface. Atomic layer deposited Al_2O_3 is known to remain amorphous in higher temperatures compared to our annealing temperature of 420 °C [26]; hence, it was unlikely that pore formation was originating from crystallization of Al_2O_3. Depending on the reference [35–38], crystallization

of amorphous ALD overcoating require approximately 700–900 °C. Therefore, we suggest that the enhanced performance of overcoated catalysts result from milder changes taking place during thermal annealing. Previous studies have shown that already during thermal annealing at lower temperatures, ALD overcoatings densify, resulting in mass loss and change of chemical composition [37,38]. Mass is lost mainly due to oxygen, hydrogen, and carbon residue evaporation, causing overcoat densification and thinning. These transformations together change the chemical reaction environment on the catalyst surface, affecting the activity and selectivity of the catalyst, as well as stabilizing and protecting cobalt particles from sintering and migration.

It is reported that in the beginning of the ALD process, overcoating prefers to grow on low-coordination sites leaving other areas of the substrate with thinner coating [25,39,40]. Due to the FT reaction complexity and challenge to characterize alumina overcoating on alumina supported catalyst, this low-coordination site favoring effect on catalyst performance remains unclear (see Supplementary Materials for scanning electron (SEM) and transmission electron microscopy (TEM) images). Nevertheless, our results show overall activity increase for catalyst + 35c + TA and having particle size with structure-insensitive reaction rate [11,38,41] (11 nm, Table 2), indeed it must be the overcoat having effect on the catalyst activity and selectivity. Our assumption was that increased activity relates to the overcoating opening at the high activity locations, creating a porous film for enhanced hydrogenation activity. In addition, lower activity sites might have been modified towards increased activity. In literature, terrace site lower specific activity is attributed to a slower intermediate (CH_x) hydrogenation and decreased CO dissociation [42]. ALD overcoat reformation during thermal annealing may create defects on terrace sites, resulting in conditions similar to higher activity sites. This assumption could be supported with a recent study by Pestman et al. [30], who presented that a shortage of stepped sites would limit hydrocarbon formation due to insufficient CO dissociation locations. They proposed that if enough CO dissociation step sites are present, structure-insensitive hydrogenation will dictate the overall reaction rate. As hydrogenation is a structure-insensitive reaction step, a porous overcoat could generate better activity via increased CO dissociation sites on otherwise low activity surfaces (e.g., terraces).

3. Experimental

3.1. Catalyst Preparation

Co-Pt-Si/γ-Al_2O_3 catalyst was prepared by incipient wetness co-impregnation of cobalt nitrate ($Co(NO_3)_2{\cdot}6H_2O$) and platinum nitrate ($Pt(NO_3)_2$). Tetraethoxysilane ($C_8H_{20}SiO_4$) was impregnated in a following separate step on γ-Al_2O_3 support (Puralox SCCa 5-150 Brunsbüttel, Germany), S_{BET} 140 $m^2\ g^{-1}$, V_{pore} 0.46 Nml g^{-1} and d_{pore} 13.2 nm). The catalyst was dried in a rotary evaporator (80 °C, 60 min) and calcination was carried out under continuous air flow at 250 °C (ramp 2 °C min^{-1}, 1 Nl $gcat^{-1}$ h^{-1}) for 4 h. After the calcination, the catalyst was sieved, and a 50–150 µm particle size fraction was collected. The resulting catalyst had 21.4 wt % cobalt, 0.2 wt % platinum, and 1.6 wt % silicon. Platinum promoter assisted hydrogen reduction and silicon was added to prevent support leaching [43]. From here on, catalyst refers to Co-Pt-Si/γ-Al_2O_3 and ALD overcoating and thermal annealing is labelled in short for example catalyst + 35c + TA, where 35 denotes for the number of ALD cycles.

The prepared catalyst batch was divided into two separate sets. The first set was used as such in the Fischer–Tropsch tubular reactor experiments, and the second set was overcoated by ALD with 15, 25, 35, and 40 cycles of Al_2O_3 at 150 °C. ALD coatings for approximately 3-g batches were performed using an ALD Picosun R-200 tool and POCA powder coating system. Due to the porosity of the catalyst powder, the sequential micro pulsing set up was used for enhancing the precursor diffusion. In this set up, several consecutive short pulses of the same precursor are fed to the reactor before long purging steps. Furthermore, substrate agitation was carried out with an ultrasound system, included in the POCA system. N_2 (purity 99.999%) from liquid nitrogen gas was used

as a carrier gas. Si (100) (Siltronic Corporation) was used as the substrate for measuring reference thicknesses, and Al_2O_3 overcoatings were prepared from TMA (>98%, Strem Chemicals, Newburyport, MA, USA) as a metal precursor and deionized water.

Before reduction, the ALD overcoated catalysts were annealed in a tubular reactor at atmospheric pressure, N_2 flow 40 Nml min^{-1} (~0.6 g) and with a temperature program from room temperature to 420 °C at 4 °C min^{-1}. Immediately after reaching terminal temperature, cool down was started with an N_2 flow of 80 Nml min^{-1} and the temperature was decreased to 150 °C. Reduction was started by adding a hydrogen flow of 100 Nml min^{-1} with temperature ramp of 5 °C min^{-1} to 400 °C. Finally, after 12 h reduction, the reactor was cooled to 180 °C (under H_2 flow of 20 mL min^{-1}) and the catalyst was ready for the reaction experiment.

3.2. Catalyst Characterization

3.2.1. Nitrogen Adsorption and Desorption

To determine the catalyst surface area, pore volume and average pore diameter, nitrogen adsorption–desorption isotherms were measured at liquid nitrogen temperature (77 K) with a Micromeritics 3Flex 3500 instrument (Atlanta, GA, USA). Before isotherm measurement, samples (~0.1 g) were outgassed with a VacPrep instrument at 200 °C for 12 h.

The catalyst surface area was estimated using the Brunauer–Emmett–Teller (BET) [44] equation, and the Barrett–Joyner–Halenda (BJH) [45] method was used for total pore volume and average pore diameter determination. Average pore diameter was evaluated from the nitrogen desorption branch.

3.2.2. Temperature-Programmed Reduction (TPR)

Catalyst sample reducibility measurements were performed by H_2 temperature-programmed reduction with a Micromeritics 3Flex 3500 (Atlanta, GA, USA) instrument. Prior to analysis, the sample (~0.1 g) was packed into a quartz U-tube reactor and outgassed in a flow of He at 200 °C for 2 h. After inert gas treatment, the temperature was decreased to 30 °C and reduction was started with 10% H_2 in Ar (50 Nml min^{-1}) at a ramp rate of 10 °C min^{-1} until 900 °C. During the temperature program, hydrogen consumption was monitored with a thermal conductivity detector (TCD) and cold trap (liquid nitrogen/isopropanol mixture) was used to remove residual water before analysis.

3.2.3. In-Situ X-ray Diffraction

Catalyst XRD diffraction patterns were measured with a PANalytical X'Pert PRO MPD Alfa-1 diffractometer (Malvern, UK) (CuKα1 radiation at 45 kV/40 mA, λ1 = 1.54060 Å) and Anton-Paar HTK 1200N furnace with fixed divergence, anti-scatter slits and 10 mm mask. The scans were performed in the 2θ range from 30° to 47°, with a step size 0.039°. In-situ measurement was initiated by flowing in nitrogen (40 Nml min^{-1}) at 25 °C. After 1 h of nitrogen flushing, thermal annealing was performed as described earlier. When thermal annealing reached temperature of 420 °C, the XRD chamber was cooled down to 150 °C under nitrogen flow (80 Nml min^{-1}). At 150 °C, the nitrogen feed was switched to reducing gas (10 % H_2 in N_2, 100 Nml min^{-1}) and the reduction was started with 5 °C min^{-1} to 400 °C (hold 6 h). In-situ XRD diffractograms were collected at 25 °C before annealing, at 420 °C right after annealing, at 150 °C before reducing gas feed, at 150 °C before starting reduction temperature ramp, and every hour after reaching 400 °C.

Average cobalt oxide crystallite size was determined before thermal annealing and reduction with Scherrer's equation [46] using the highest intensity (311) Co_3O_4 peak found at 2θ = 36.9° [47]

$$d(Co_3O_4) = \times \frac{180^\circ}{\pi} \quad (4)$$

where 0.89 is the K-factor, λ is the X-ray wavelength, and B is the full width at half maximum (FWHM) of the cobalt oxide diffraction peak.

Co^0 peak found at 2θ = 44.2° (Cubic Co, JCPDS card no. 00-015-0806) was used to determine the metallic cobalt particle size for catalyst without overcoating and catalyst + 35c + TA.

3.2.4. Static H_2-Chemisorption and O_2-Titration

Hydrogen adsorption isotherms were measured with a Micromeritics 3Flex 3500 instrument. Catalyst samples (~0.1 g) were evacuated at 40 °C for 1 h and reduced in-situ with flowing hydrogen at 400 °C for 12 h (ramp rate 2 °C min^{-1}). After reduction, the samples were cooled in vacuum (<0.1 mm Hg) to 35 °C. The adsorption isotherms were obtained at 35 °C between 2.1–446 mm Hg. Equation (5) was used to determine the cobalt metal dispersion [48], where one hydrogen molecule was assumed to interact with two cobalt surface atoms [6,48]. The calculated dispersion percentage was then used to estimate the cobalt particle size (nm) in Equation (6) by assuming spherical and uniform metal particles with a site density of 14.6 atoms nm^{-2} [49].

$$Dispersion = 1.18\chi/EOR/M\% \quad (5)$$

where χ is H_2 uptake (μmol $gcat^{-1}$) from chemisorption measurement, extent of reduction (EOR) is from TPR measurement (Table 3), and M% is the percentage of active metal by weight as grams of metal per gram of sample.

$$Cobalt\ particle\ size\ (\mathrm{nm}) = \frac{96.2}{D(\%)} \quad (6)$$

Prior to oxygen titration with calibrated pulses of O_2, the catalyst sample was reduced in the conditions described above for the static H_2-chemisorption experiment. Before starting oxygen pulsing, the temperature was increased from reduction temperature to 425 °C and O_2 pulses were introduced to a known sample amount. O_2 pulses were added until no consumption was detected by thermal conductive detector (TCD). The extent of reduction was calculated by assuming Co^0 to Co_3O_4 stoichiometric conversion.

3.3. Catalyst Testing

Fischer–Tropsch experiments were performed in a tubular fixed-bed reactor system (Hastelloy C, 9.1 mm i.d.) at a temperature of 200 °C, pressure 20 bar and H_2/CO ratio 2.0. Detailed equipment description can be found elsewhere [27]. To minimize temperature gradients over the catalyst bed, ~0.6 g of sample (50–150 μm) was diluted with ~2.0 g of silicon carbide (105 μm). Prior to CO addition, reactor was pressurized with H_2 and N_2. After pressure was stabilized, CO addition was started. Initial reaction temperature runaway was prevented by slow addition of CO at 180 °C. After desired inlet gas composition was reached (H_2 60 vol %, CO 30 vol %, N_2 10 vol % internal standard), the temperature was increased to 200 °C. Gas hourly space velocity was altered during the experiment to achieve at least three different CO conversion levels in the range of 5–15%.

Heavy Fischer–Tropsch products were separated in a hot trap (100 °C, at reaction pressure), while water and lighter hydrocarbons (C_6–C_{20}) were collected in a liquid-liquid-gas separator at 10 °C. The remaining effluent gas compounds (H_2, N_2, CO, CO_2, C_1-C_{14} hydrocarbons) were analyzed with an on-line gas chromatograph (Shimadzu GC-2014, Kyoto, Japan) with a thermal conductivity (TCD) and flame ionization detectors (FID). H_2, N_2, CO, CO_2, and CH_4 were analyzed with a TCD line consisting of a precolumn (Porapak-Q, 1 mm i.d. × 1.8 m) and an analytical column (Carboxen-1000, 1 mm i.d. × 2.5 m). The precolumn was adapted to facilitate backflush of heavy hydrocarbons enabling only light compounds entering the TCD. The remaining hydrocarbon products from C_1 to C_{14} as well as C_1–C_9 n-alcohols were separated and analyzed with a DB-1 capillary column (i.d. 0.25 mm × 60 m × 1 μm) and FID.

Fischer–Tropsch oil and wax samples were analyzed with offline methods after sample collection. Hydrocarbon analyses for C_6-C_{20} and C_1-C_9 n-alcohols were performed with a Shimadzu GC-2014 (Rxi-5HT, i.d. 0.32 mm × 30 m × 0.10 μm df) and heavy hydrocarbons ranging from C_{10} to C_{80+} were analyzed with a high-temperature HP5890 gas chromato-

graph with an on-column injection port and a CP-SimDist UltiMetal separation column (i.d. 0.53 mm × 10 m × 0.17 µm df, 1 m retention gap).

4. Conclusions

A catalyst with 21.4 wt % cobalt, 0.2 wt % platinum, and 1.6 wt % silicon on a γ-Al_2O_3 support was prepared by incipient wetness co-impregnation and overcoated with ALD deposited Al_2O_3. Prepared and thermally annealed catalysts were studied in a tubular reactor under relevant Fischer–Tropsch conditions (200 °C, 20 bar, H_2/CO ratio 2) and characterized by several methods. A positive effect on catalyst activity was observed with 35 cycle ALD catalyst without compromising selectivity towards heavy hydrocarbons. Our results indicate that the ALD overcoat alters the chemical environment on catalyst surface resulting in modified activity and selectivity. In this study, we showed that thermal treatment (420 °C) for ALD overcoat is required to prepare a FT catalyst with modified surface structure leading to enhanced activity and selectivity. However, more thorough characterization of the ALD surface structure and reactions are needed to confirm the hypothesis presented in this study. ALD catalyst research has been very promising and successful during the past decade, but more fundamental research and experiments are still needed in addition to efforts for scaling-up the processes for industrial manufacturing.

Supplementary Materials: The following tables are available online at https://www.mdpi.com/article/10.3390/catal11060672/s1. scanning electron microscope (SEM) and transmission electron microscopy (TEM) images for catalyst sample with and without ALD overcoating; product selectivity as olefin to paraffin ratio.

Author Contributions: The manuscript was written through contributions of all authors. Methodology, formal analysis, and investigation, N.H., L.K., and P.E.; project administration and supervision, M.R. and M.P. All authors contributed to the discussion of the experimental results and the commenting and editing of the manuscript. All authors have read and agreed to the published version of the manuscript.

Funding: This research was funded by European Union's Horizon 2020 research and innovation program under grant agreement no. 768543 (ICO2CHEM project-From industrial CO_2 streams to added value Fischer–Tropsch chemicals). M.P. acknowledges funding from the Academy of Finland by the profiling action on Matter and Materials, grant no. 318913.

Acknowledgments: Mikko J. Heikkilä (University of Helsinki), Unto Tapper (VTT), Tyko Viertiö (VTT), Mirja Muhola (VTT), Noora Kaisalo (VTT).

Conflicts of Interest: The authors declare no conflict of interest.

References

1. Wood, D.; Nwaoha, C.; Towler, B.F. Gas-to-liquids (GTL): A review of an industry offering several routes for monetizing natural gas. *J. Nat. Gas Sci. Eng.* **2012**, *9*, 196–208. [CrossRef]
2. Dry, M.E. The Fischer–Tropsch process: 1950–2000. *Catal. Today* **2002**, *71*, 227–241. [CrossRef]
3. O'Neill, B.J.; Jackson, D.H.K.; Lee, J.; Canlas, C.; Stair, P.C.; Marshall, C.L.; Elam, J.W.; Kuech, T.F.; Dumesic, J.A.; Huber, G.W. Catalyst Design with Atomic Layer Deposition. *ACS Catal.* **2015**, *5*, 1804–1825. [CrossRef]
4. De Klerk, A. Transport Fuel. In *Future Energy*; Elsevier: London, UK, 2020; pp. 199–226.
5. Garces, L.J.; Hincapie, B.; Zerger, R.; Suib, S.L. The Effect of Temperature and Support on the Reduction of Cobalt Oxide: An in Situ X-ray Diffraction Study. *J. Phys. Chem. C* **2015**, *119*, 5484–5490. [CrossRef]
6. Borg, Ø.; Eri, S.; Blekkan, E.A.; Storsæter, S.; Wigum, H.; Rytter, E.; Holmen, A. Fischer–Tropsch synthesis over γ-alumina-supported cobalt catalysts: Effect of support variables. *J. Catal.* **2007**, *248*, 89–100. [CrossRef]
7. Jacobs, G.; Das, T.K.; Zhang, Y.; Li, J.; Racoillet, G.; Davis, B.H. Fischer–Tropsch synthesis: Support, loading, and promoter effects on the reducibility of cobalt catalysts. *Appl. Catal. A Gen.* **2002**, *233*, 263–281. [CrossRef]
8. Dinse, A.; Aigner, M.; Ulbrich, M.; Johnson, G.R.; Bell, A.T. Effects of Mn promotion on the activity and selectivity of Co/SiO_2 for Fischer–Tropsch Synthesis. *J. Catal.* **2012**, *288*, 104–114. [CrossRef]
9. Gavrilović, L.; Save, J.; Blekkan, A. The Effect of Potassium on Cobalt-Based Fischer–Tropsch Catalysts with Different Cobalt Particle Sizes. *Catalysts* **2019**, *9*, 351. [CrossRef]
10. Vada, S.; Hoff, A.; Schanke, D.; Holmén, A. Fischer-Tropsch synthesis on supported cobalt catalysts promoted by platinum and rhenium. *Top. Catal.* **1995**, *2*, 155–162. [CrossRef]

11. Breejen, J.P.D.; Radstake, P.B.; Bezemer, G.L.; Bitter, J.H.; Frøseth, V.; Holmen, A.; De Jong, K.P. On the Origin of the Cobalt Particle Size Effects in Fischer−Tropsch Catalysis. *J. Am. Chem. Soc.* **2009**, *131*, 7197–7203. [CrossRef]
12. Fischer, N.; Clapham, B.; Feltes, T.; Claeys, M. Cobalt-Based Fischer–Tropsch Activity and Selectivity as a Function of Crystallite Size and Water Partial Pressure. *ACS Catal.* **2014**, *5*, 113–121. [CrossRef]
13. Bezemer, G.L.; Bitter, J.H.; Kuipers, H.P.; Oosterbeek, H.; Holewijn, J.E.; Xu, X.; Kapteijn, F.; Van Dillen, A.J.; De Jong, K.P. Cobalt Particle Size Effects in the Fischer−Tropsch Reaction Studied with Carbon Nanofiber Supported Catalysts. *J. Am. Chem. Soc.* **2006**, *128*, 3956–3964. [CrossRef]
14. Pagan-Torres, Y.; Gallo, J.M.R.; Wang, D.; Pham, H.N.; Libera, J.A.; Marshall, C.L.; Elam, J.W.; Datye, A.K.; Dumesic, J.A. Synthesis of Highly Ordered Hydrothermally Stable Mesoporous Niobia Catalysts by Atomic Layer Deposition. *ACS Catal.* **2011**, *1*, 1234–1245. [CrossRef]
15. Muylaert, I.; Musschoot, J.; Leus, K.; Dendooven, J.; Detavernier, C.; Van Der Voort, P. Atomic Layer Deposition of Titanium and Vanadium Oxide on Mesoporous Silica and Phenol/Formaldehyde Resins-the Effect of the Support on the Liquid Phase Epoxidation of Cyclohexene. *Eur. J. Inorg. Chem.* **2011**, *2012*, 251–260. [CrossRef]
16. Onn, T.M.; Küngas, R.; Fornasiero, P.; Huang, K.; Gorte, R.J. Atomic Layer Deposition on Porous Materials: Problems with Conventional Approaches to Catalyst and Fuel Cell Electrode Preparation. *Inorganics* **2018**, *6*, 34. [CrossRef]
17. Strempel, V.E.; Knemeyer, K.; D'Alnoncourt, R.N.; Driess, M.; Rosowski, F. Investigating the Trimethylaluminium/Water ALD Process on Mesoporous Silica by In Situ Gravimetric Monitoring. *Nanomaterials* **2018**, *8*, 365. [CrossRef]
18. Elam, J.W.; Routkevitch, D.; Mardilovich, P.P.; George, S.M. Conformal Coating on Ultrahigh-Aspect-Ratio Nanopores of Anodic Alumina by Atomic Layer Deposition. *Chem. Mater.* **2003**, *15*, 3507–3517. [CrossRef]
19. Sarnello, E.; Lu, Z.; Seifert, S.; Winans, R.E.; Li, T. Design and Characterization of ALD-Based Overcoats for Supported Metal Nanoparticle Catalysts. *ACS Catal.* **2021**, *11*, 2605–2619. [CrossRef]
20. Lu, J.; Liu, B.; Greeley, J.P.; Feng, Z.; Libera, J.A.; Lei, Y.; Bedzyk, M.J.; Stair, P.C.; Elam, J.W. Porous Alumina Protective Coatings on Palladium Nanoparticles by Self-Poisoned Atomic Layer Deposition. *Chem. Mater.* **2012**, *24*, 2047–2055. [CrossRef]
21. Lee, J.; Jackson, D.H.K.; Li, T.; Winans, R.E.; Dumesic, J.A.; Kuech, T.F.; Huber, G.W. Enhanced stability of cobalt catalysts by atomic layer deposition for aqueous-phase reactions. *Energy Environ. Sci.* **2014**, *7*, 1657. [CrossRef]
22. Ma, Z.; Brown, S.; Howe, J.Y.; Overbury, S.H.; Dai, S. Surface Modification of Au/TiO_2 Catalysts by SiO_2 via Atomic Layer Deposition. *J. Phys. Chem. C* **2008**, *112*, 9448–9457. [CrossRef]
23. Liang, X.; Li, J.; Yu, M.; McMurray, C.N.; Falconer, J.L.; Weimer, A.W. Stabilization of Supported Metal Nanoparticles Using an Ultrathin Porous Shell. *ACS Catal.* **2011**, *1*, 1162–1165. [CrossRef]
24. Liang, X.; Evanko, B.W.; Izar, A.; King, D.M.; Jiang, Y.-B.; Weimer, A.W. Ultrathin highly porous alumina films prepared by alucone ABC molecular layer deposition (MLD). *Microporous Mesoporous Mater.* **2013**, *168*, 178–182. [CrossRef]
25. Lu, J.; Fu, B.; Kung, M.C.; Xiao, G.; Elam, J.W.; Kung, H.H.; Stair, P.C. Coking- and Sintering-Resistant Palladium Catalysts Achieved Through Atomic Layer Deposition. *Science* **2012**, *335*, 1205–1208. [CrossRef] [PubMed]
26. O'Neill, B.J.; Jackson, D.H.K.; Crisci, A.J.; Farberow, C.A.; Shi, F.; Alba-Rubio, A.C.; Lu, J.; Dietrich, P.J.; Gu, X.; Marshall, C.L.; et al. Stabilization of Copper Catalysts for Liquid-Phase Reactions by Atomic Layer Deposition. *Angew. Chem. Int. Ed.* **2013**, *52*, 13808–13812. [CrossRef]
27. Marchese, M.; Heikkinen, N.; Giglio, E.; Lanzini, A.; Lehtonen, J.; Reinikainen, M. Kinetic Study Based on the Carbide Mechanism of a Co-Pt/γ-Al_2O_3 Fischer–Tropsch Catalyst Tested in a Laboratory-Scale Tubular Reactor. *Catalysts* **2019**, *9*, 717. [CrossRef]
28. Puurunen, R.L. Surface chemistry of atomic layer deposition: A case study for the trimethylaluminum/water process. *J. Appl. Phys.* **2005**, *97*, 121301. [CrossRef]
29. Richard, L.A.; Moreau, P.; Rugmini, S.; Daly, F. Fischer-Tropsch performance correlated to catalyst structure: Trends in activity and stability for a silica-supported cobalt catalyst. *Appl. Catal. A Gen.* **2013**, *464–465*, 200–206. [CrossRef]
30. Pestman, R.; Chen, W.; Hensen, E.J. Insight into the Rate-Determining Step and Active Sites in the Fischer–Tropsch Reaction over Cobalt Catalysts. *ACS Catal.* **2019**, *9*, 4189–4195. [CrossRef]
31. Breejen, J.P.D.; Sietsma, J.R.; Friedrich, H.; Bitter, J.H.; De Jong, K.P. Design of supported cobalt catalysts with maximum activity for the Fischer–Tropsch synthesis. *J. Catal.* **2010**, *270*, 146–152. [CrossRef]
32. Nabaho, D.; Niemantsverdriet, J.H.; Claeys, M.; van Steen, E. Hydrogen spillover in the Fischer–Tropsch synthesis: An analysis of gold as a promoter for cobalt–alumina catalysts. *Catal. Today* **2016**, *275*, 27–34. [CrossRef]
33. Van De Loosdrecht, J.; Barradas, S.; Caricato, E.; Ngwenya, N.; Nkwanyana, P.; Rawat, M.; Sigwebela, B.; Van Berge, P.; Visagie, J. Calcination of Co-Based Fischer–Tropsch Synthesis Catalysts. *Top. Catal.* **2003**, *26*, 121–127. [CrossRef]
34. Nabaho, D. Hydrogen Spillover in the Fischer-Tropsch Synthesis: The Role of Platinum and Gold as Promoters in Co-Balt-Based Catalysts. Ph.D. Thesis, University of Cape Town, Cape Town, South Africa, 2015.
35. Broas, M.; Kanninen, O.; Vuorinen, V.; Tilli, M.; Paulasto-Kröckel, M. Chemically Stable Atomic-Layer-Deposited Al_2O_3 Films for Processability. *ACS Omega* **2017**, *2*, 3390–3398. [CrossRef]
36. Broas, M.; Lemettinen, J.; Sajavaara, T.; Tilli, M.; Vuorinen, V.; Suihkonen, S.; Paulasto-Kröckel, M. In-situ annealing characterization of atomic-layer-deposited Al_2O_3 in N_2, H_2 and vacuum atmospheres. *Thin Solid Films* **2019**, *682*, 147–155. [CrossRef]
37. Cimalla, V.; Baeumler, M.; Kirste, L.; Prescher, M.; Christian, B.; Passow, T.; Benkhelifa, F.; Bernhardt, F.; Eichapfel, G.; Himmerlich, M.; et al. Densification of Thin Aluminum Oxide Films by Thermal Treatments. *Mater. Sci. Appl.* **2014**, *05*, 628–638. [CrossRef]

38. Jakschik, S.; Schroeder, U.; Hecht, T.; Gutsche, M.; Seidl, H.; Bartha, J.W. Crystallization behavior of thin ALD-Al_2O_3 films. *Thin Solid Films* **2003**, *425*, 216–220. [CrossRef]
39. Lu, J.; Liu, B.; Guisinger, N.P.; Stair, P.C.; Greeley, J.P.; Elam, J.W. First-Principles Predictions and in Situ Experimental Validation of Alumina Atomic Layer Deposition on Metal Surfaces. *Chem. Mater.* **2014**, *26*, 6752–6761. [CrossRef]
40. Feng, H.; Lu, J.; Stair, P.C.; Elam, J.W. Alumina Over-coating on Pd Nanoparticle Catalysts by Atomic Layer Deposition: Enhanced Stability and Reactivity. *Catal. Lett.* **2011**, *141*, 512–517. [CrossRef]
41. Ge, A.Q.; Neurock, M. Adsorption and Activation of CO over Flat and Stepped Co Surfaces: A First Principles Analysis. *J. Phys. Chem. B* **2006**, *110*, 15368–15380. [CrossRef]
42. Den Breejen, J.P. Cobalt Particle Size Effects in Catalysis. Ph.D. Thesis, Utrecht University, Utrecht, The Netherlands, 2010; ISBN: 978-90-6464-377-4
43. Rytter, E.; Holmen, A. On the support in cobalt Fischer–Tropsch synthesis—Emphasis on alumina and aluminates. *Catal. Today* **2016**, *275*, 11–19. [CrossRef]
44. Brunauer, S.; Emmett, P.H.; Teller, E. Adsorption of Gases in Multimolecular Layers. *J. Am. Chem. Soc.* **1938**, *60*, 309–319. [CrossRef]
45. Barrett, E.P.; Joyner, L.G.; Halenda, P.P. The Determination of Pore Volume and Area Distributions in Porous Substances. I. Computations from Nitrogen Isotherms. *J. Am. Chem. Soc.* **1951**, *73*, 373–380. [CrossRef]
46. Scherrer, P. Bestimmung der Grosse und der inneren Struktur von Kolloidterilchen mittels Rontgestrahlen. *Nachr. Ges. Wiss. Göttingen* **1918**, *1918*, 98–100. (In Germany)
47. Wang, Z.L. Characterization of nanophase materials. *Part. Part. Syst. Charact.* **2001**, *18*, 142–165. [CrossRef]
48. Cook, K.M.; Poudyal, S.; Miller, J.T.; Bartholomew, C.H.; Hecker, W.C. Reducibility of alumina-supported cobalt Fischer–Tropsch catalysts: Effects of noble metal type, distribution, retention, chemical state, bonding, and influence on cobalt crystallite size. *Appl. Catal. A Gen.* **2012**, *449*, 69–80. [CrossRef]
49. Jones, R.D.; Bartholomew, C.H. Improved flow technique for measurement of hydrogen chemisorption on metal catalysts. *Appl. Catal.* **1988**, *39*, 77–88. [CrossRef]